Journal of Materials Chemistry A

ROYAL SOCIETY OF CHEMISTRY

PAPER

View Article Online
View Journal | View Issue

Cite this: J. Mater. Chem. A, 2022, 10, 19699

$BiVO_4$ quadrangular nanoprisms with highly exposed {101} facets for selective photocatalytic oxidation of benzylamine†

Min Lv,[a] Fengxia Tong,[a] Zeyan Wang,[a] Yuanyuan Liu,[a] Peng Wang,[a] Hefeng Cheng,[a] Ying Dai,[b] Zhaoke Zheng *[a] and Baibiao Huang[a]

Photocatalytic oxidation of amines to high value-added imines is crucial but challenging. The adsorption ability to reactant molecules and the charge separation ability are important factors affecting the reactivity. Different facets of monoclinic $BiVO_4$ (m-$BiVO_4$) have varied electronic structures, leading to differences in the adsorption ability and charge separation ability. Thus, tailoring the exposed facets is a promising strategy to optimize the reactivity. Herein, the density functional theory (DFT) calculations demonstrate that for m-$BiVO_4$, both the benzylamine ($BnNH_2$) adsorption ability and charge separation ability of {101} facets were stronger than those of {110} facets. These results motivate us to synthesize m-$BiVO_4$ quadrangular nanoprisms (Q-$BiVO_4$) with highly exposed {101} facets through a colloidal two-phase method. Q-$BiVO_4$ exhibits highly enhanced charge separation efficiency and excellent photocatalytic performance for oxidizing $BnNH_2$ to *N*-benzylidenebenzylamine (*N*-BB). More impressively, the efficient charge transfer between Q-$BiVO_4$ and $BnNH_2$ was directly confirmed *via* single-particle spectroscopy *in situ*. This work provides direct evidence to deeply understand the interaction between Q-$BiVO_4$ and the reactant molecules and provides insights for rational design of photocatalysts with specific exposed facets for selective oxidation of amines.

Received 6th March 2022
Accepted 31st March 2022

DOI: 10.1039/d2ta01758j

rsc.li/materials-a

[a]State Key Laboratory of Crystal Materials, Shandong University, Jinan 250100, China. E-mail: zkzheng@sdu.edu.cn
[b]School of Physics, Shandong University, Jinan 250100, China

† Electronic supplementary information (ESI) available. See DOI: 10.1039/d2ta01758j

Dr Zhaoke Zheng is a Professor at State Key Laboratory of Crystal Materials at Shandong University. He received his BS (2007) and PhD (2012) at Shandong University, and joined Osaka University as a JSPS fellow in 2013. Afterwards, he moved to the University of New South Wales as a postdoc and later joined University of Konstanz as an Alexander von Humboldt (AvH) fellow. He was appointed as a European Research Council (ERC) remote referee in 2020, and has won the Distinguished Young Scholars of Shandong Province Science Foundation award. His research interests focus on plasmonic photocatalysis and mechanism study by single-particle spectroscopy.

Introduction

Imines are important versatile intermediates widely used in the fields of pharmaceutical synthesis, agriculture, and the chemical industry.[1–3] The conventional synthesis of imines usually involves the condensation of amines and carbonyl compounds, which requires oxidants, corrosive chemicals, and heating conditions.[4,5] However, traditional oxidants are harmful to the environment and uneconomical.[6–8] Moreover, the extremely high reactivity of aldehydes makes it difficult to control the reaction.[9] Therefore, more environmentally friendly and milder approaches are highly desired for the synthesis of imines. On the one hand, a catalytic system using molecular oxygen as an oxidant instead of traditional chemical oxidants is an ideal way in view of green chemistry.[1–3] On the other hand, in recent years, the photocatalytic organic transformation as a promising approach has attracted growing interest, and can effectively convert solar energy into chemical energy. A great number of photocatalysts have been investigated for the oxidation of amines to imines such as Nb_2O_5,[2] $CuWO_4$,[10] g-C_3N_4,[11] Au/TiO_2,[12] and BiOX (X = Cl, Br).[13,14] However, some of the catalysts respond only to ultraviolet light and still have the problems of low product yield and selectivity.

Monoclinic $BiVO_4$, as a visible-light-responsive catalyst, has received widespread attention due to its non-toxicity, low price and suitable band gap.[15–17] However, the rapid recombination

of photogenerated electron–hole pairs and weak surface adsorption ability in m-$BiVO_4$ still restrict the photocatalytic performance.[18–20] Various strategies such as semi-conductor coupling,[18] element doping,[21] and cocatalyst deposition[22] have been employed to improve the photocatalytic performance. Nonetheless, the photocatalytic performance of pristine m-$BiVO_4$ is still not impressive. In this regard, there is a great need to develop effective strategies to enhance the reactivity of m-$BiVO_4$. As is well known, the photocatalytic performance of materials depends not only on their crystal structure, but also on the morphology and exposed facets. More recently, an increasing exploration has been conducted on the facet engineering of m-$BiVO_4$.[15,23–26] Studies have shown that due to the distinct atomic arrangements and configurations, different facets of m-$BiVO_4$ have varied electronic structures, which leads to different properties of crystal facets in the ability to adsorb/desorb reactive molecules and the carrier separation ability in the photocatalytic process.[15,27,28] Therefore, a rational design and well-controlled synthesis of m-$BiVO_4$ with specific exposed facets and inquiring how the morphologies and crystal facets affect the adsorption of reactive molecules and the charge separation are of great significance and urgently desired.

Herein, based on density functional theory (DFT) calculations, we theoretically demonstrated that {101} facets of m-$BiVO_4$ not only possessed stronger benzylamine ($BnNH_2$) adsorption ability but also had better carrier separation ability than the common {110} facets. The reason why the {110} facets were chosen for comparison was that the typical low-index {110} facets are hole-accumulated surfaces[24] and can participate in the photocatalytic $BnNH_2$ oxidation reaction. Our DFT calculations revealed that the greater overlap degree between the interacting orbitals and the lighter effective masses of photogenerated electrons and holes of {101} facets than those of {110} facets made {101} facets more active for charge transfer. Moreover, the charge transfer mode of Bi–O–Bi between (010) and (101) facets is much easier than that of Bi–O–V between (010) and (110) facets, endowing the former with stronger charge transfer ability.

Inspired by these results, monoclinic $BiVO_4$ quadrangular nanoprisms (Q-$BiVO_4$) with highly exposed {101} facets were successfully synthesized using a precisely controlled colloidal two-phase method. Q-$BiVO_4$ exhibited a superior photocatalytic activity for $BnNH_2$ oxidation with a conversion efficiency of 98.3%, about 2.03 fold higher than that of conventional decahedron $BiVO_4$ (D-$BiVO_4$) with highly exposed {110} facets. The photocurrent density of Q-$BiVO_4$ was 0.511 mA cm^{-2} at 1.23 V_{RHE}, about 16.5 times higher than that of D-$BiVO_4$. More importantly, the interaction between Q-$BiVO_4$, acetonitrile (ACN) and $BnNH_2$ was tracked by using single-particle spectra *in situ*, revealing the efficient charge transfer between Q-$BiVO_4$ and $BnNH_2$, and ACN only acted as a solvent. This work provides direct evidence for charge transfer between Q-$BiVO_4$ and the reactant molecules *via* single-particle PL measurement and offers an avenue to design efficient photocatalysts for organic transformations.

Experimental

Materials

1-Octadecene (ODE, 90%), oleylamine (OLA, 80–90%), oleic acid (OA), benzylamine (99.0%), acetonitrile (99.0%, GC) and 1,4-benzoquinone (BQ, 99%) were purchased from Aladdin Industrial Corporation, China. Bismuth nitrate pentahydrate ($Bi(NO_3)_3 \cdot 5H_2O$, 99.0%), ammonium metavanadate (NH_4VO_3, 99%), HNO_3 aqueous solution (65–68%), ammonium hydroxide ($NH_3 \cdot H_2O$, 25%), *n*-hexane, ethanol (99.5%), carbon tetrachloride (CCl_4, 99.5%) and ammonium oxalate (AO) were purchased from the Sinopharm Chemical Reagent Co., Ltd (Shanghai, China). Nano-$BiVO_4$ was purchased from the Energy Chemical Reagent Co., Ltd (Shanghai, China). All of the reagents were used as received without further purification.

Preparation of Q-$BiVO_4$

Q-$BiVO_4$ was synthesized by a convenient colloidal two-phase method. Typically, 1.0 mmol of $Bi(NO_3)_3 \cdot 5H_2O$, 2 mL of OLA, 2 mL of OA and 20 mL of ODE were added in a three-neck flask. Before heating, the system was degassed by purging N_2 for 30 min. Then the flask was heated to 170 °C under vigorous stirring and an N_2 atmosphere until $Bi(NO_3)_3$ was completely dissolved. Finally, a transparent solution was obtained. In another vessel, 2.0 mmol NH_4VO_3 was dissolved in a mixture of 4 mL HNO_3 and 20 mL H_2O. Then, the NH_4VO_3 solution was slowly injected into the above flask containing dissolved $Bi(NO_3)_3$ as the temperature dropped from 170 °C to 100 °C (about 25 min). The reaction system was stirred and refluxed at 100 °C for 30 min under an N_2 atmosphere and terminated by removing the heating source, followed by natural cooling. A mixture of *n*-hexane and ethanol was then added into the products. After the solution was stratified, the underlying aqueous solution was discarded and the remaining organic solution was centrifuged at 12 000 rpm for 3 min to discard the unreacted precursors. The resulting product was subsequently washed with hexane and ethanol and then centrifuged (12 000 rpm, 3 min) three times in total. Finally, the precipitates were freeze-dried for 12 hours.

Characterization

The morphology and structure of the samples were investigated by using a field emission scanning electron microscope (FESEM, Hitachi S-4800), transmission electron microscope (TEM, JEM-2100F) and high-resolution transmission electron microscope (HRTEM, JEM-2100F). The X-ray powder diffraction (XRD) patterns of the samples were measured on a Bruker AXS D8 diffractometer with Cu Kα radiation. Diffuse reflectance spectroscopy (DRS) of the samples was perfomed using a UV-2600 Shimadzu UV-vis spectrophotometer. X-ray photoelectron spectroscopy (XPS) was performed on a Thermo Fisher Scientific Escalab 250 spectrometer equipped with an Al Kα excitation source (1486.6 eV), and the binding energies were corrected by using the C 1s peak (284.8 eV). Raman spectra were detected by using an *in situ* confocal Raman spectrometer (LabRAM HR Evolution). The Brunauer–Emmett–Teller (BET) surface area

and pore-size distribution of the samples were measured by using a Micromeritics ASAP Kubo X1000 analyzer at liquid nitrogen temperature.

Photocatalytic experimental details

The photocatalytic oxidation of benzylamine to imine was carried out in a quartz reaction vessel. For each experiment, 10 mg of photocatalysts and 0.1 mmol of benzylamine were mixed in 5 mL of acetonitrile to form a suspension. Prior to light irradiation, the suspension was ultrasonically dispersed for 2 min and purged with O_2 for 30 min. The reaction temperature was maintained at 25 °C. The photocatalytic reactions were carried out under irradiation with a 300 W Xenon lamp (CEL-HXF300) with a 420 nm cut-off filter for 4 h. The light intensity was 0.4 W cm^{-2} during the photocatalytic $BnNH_2$ oxidation process. After the photocatalytic reaction, the photocatalysts were separated by centrifugation at 12 000 rpm for 3 min. The liquid products were analyzed by using a gas chromatograph-mass spectrometer (GC-MS-QP2010, SH-Rtx-Wax column) equipped with a flame ionization detector (FID). In the cycling stability tests, the photocatalysts after the photocatalytic reaction were centrifuged (12 000 rpm, 3 min), washed with acetonitrile and ethanol more than 3 times, and then dried in a vacuum at 60 °C for 12 h for the next test. To identify the active intermediates during the photocatalytic process, radical scavenging experiments were carried out by adding different radical scavengers. 1,4-Benzoquinone (BQ), ammonium oxalate (AO) and carbon tetrachloride (CCl_4) were employed to scavenge superoxide radicals ($^{\bullet}O_2^-$), holes (h^+) and electrons (e^-), respectively. The photocatalytic experiments in the presence of scavengers were carried out under identical conditions, except for adding 20 mM scavengers. The role of O_2 in the reaction was evaluated by replacing O_2 with argon flow. The conversion efficiency of benzylamine and selectivity of imine products were calculated using the following equations:

$$\text{Conversion } (\%) = \frac{C_0 - C_t}{C_0} \times 100\%$$

$$\text{Selectively } (\%) = \frac{C_p}{C_0 - C_t} \times 100\%$$

where C_0 is the initial concentration of benzylamine, and C_t and C_p are the concentrations of benzylamine and imine measured after the photocatalytic reaction for a specific time, respectively.

The turnover frequency (TOF) value was calculated from the following equation:

$$\text{TOF} = \frac{n_p}{n_{catal} \times t}$$

where n_p is the molar amount of imine produced, n_{catal} is the molar amount of catalyst, and t is the reaction time (h).

Single-particle PL measurements

Before the single-particle PL measurements, the quartz cover glasses were cleaned by sonication in nitric acid solution for 30 min, followed by repeated washing with deionized water 3 times. The samples were dispersed in Milli-Q ultrapure water and sonicated for 10 min. And then the well-dispersed aqueous suspensions of $BiVO_4$ were spin-coated on the clean quartz cover glasses. The single-particle PL images and spectrum of individual samples were obtained *via* a scanning confocal microscope system (PicoQuant, MicroTime 200) coupled with an Olympus IX73 inverted fluorescence microscope. The samples spin-coated on the clean quartz cover glasses were excited through an oil-immersion objective lens (Olympus, UplanSApochromat, 100×, 1.4 NA) with a 405 nm continuous wave (CW) laser controlled by using a PDL-800B driver (PicoQuant). For the decay profile, the emission of the sample was collected by using the same objective and detected by using a single photon avalanche photodiode (Micro Photon Devices, PDM 50 CT) through a dichroic beam splitter (Chroma, 405rdc) and long-pass filter (Chroma, HQ430CP). The data collected using the PicoHarp 300 TCSPC module (PicoQuant) were stored in the time-tagged time-resolved mode, recording every detected photon with its individual timing. All of the experimental data were achieved at room temperature.

Results and discussion

Previous studies have mostly focused on the m-$BiVO_4$ crystals with highly exposed low-index {010} and {110} facets.[23–26,29] Studies revealed that there are obvious differences in the carrier separation ability, the ability to adsorb reactive molecules and the surface reactivity between {010} and {110} facets,[24,28] which are closely related to the photocatalytic performance. These interesting phenomena inspired us to investigate the physicochemical properties of the low-index {101} facets based on DFT calculations. The {010} facets are the electron-accumulated surface, while {110} facets are the hole-accumulated surface and are favorable for photocatalytic $BnNH_2$ oxidation, thus the {110} facets were chosen as the control group. As shown in Fig. S1,† Bi atoms are four or five-coordinated on the (101) and (110) surfaces. Generally, m-$BiVO_4$ is constructed from a VO_4 tetrahedron and BiO_8 dodecahedron, connected by sharing an apex oxygen atom.[30] Therefore, there are uncoordinated Bi atoms exposed on these facets, which can serve as reactive sites. In order to explore the explicit interaction between $BnNH_2$ molecules and the specific exposed facets of m-$BiVO_4$, the relaxed stable structures and the corresponding adsorption energies are calculated (Fig. 1a and b). Obviously, the N atom exhibits a negative potential relative to other groups in $BnNH_2$, which may lie in the lone pair electrons of unequal sp^3 hybrid orbitals.[31,32] As a consequence, $BnNH_2$ molecules with a negatively charged N site may more easily adsorb on the surface Bi sites of m-$BiVO_4$ through the strong electrostatic interaction. The $BnNH_2$ adsorption energy on the (101) facet (−0.65 eV) is much lower than that on the (110) facet (−0.54 eV), indicating that {101} facets possess stronger $BnNH_2$ adsorption ability than {110} facets, which is favorable for the subsequent $BnNH_2$ oxidation process.

Since the charge transfer and separation ability of the exposed facets also have an effect on the photocatalytic performance, further exploration was performed from the

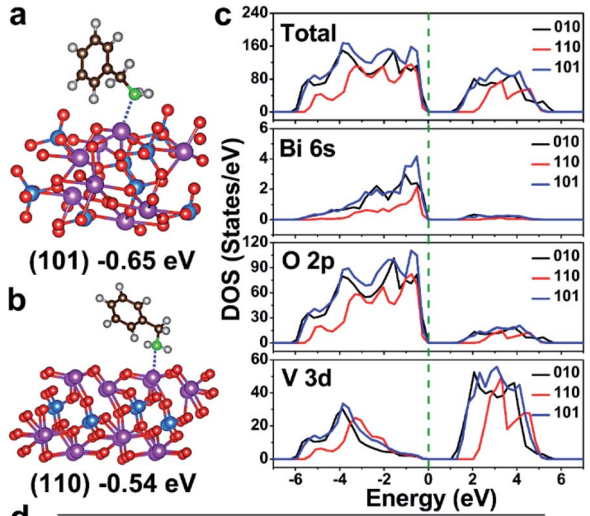

d

Crystal facets	m_h^*/m_0	m_e^*/m_0
(101)	1.173	1.179
(110)	1.191	1.198

Fig. 1 Relaxed adsorption configurations of molecular $BnNH_2$ adsorbed on the (a) (101) and (b) (110) surfaces of m-$BiVO_4$, and the corresponding adsorption energies. The red, purple, blue, green, brown, and gray balls represent oxygen, bismuth, and vanadium from $BiVO_4$, and nitrogen, carbon and hydrogen from $BnNH_2$, respectively. (c) The TDOS and the corresponding PDOSs of Bi 6s, O 2p, and V 3d for (010), (110), and (101) facets of m-$BiVO_4$. (d) The effective masses of electrons and holes of (101) and (110) facets for m-$BiVO_4$.

perspective of electronic properties. Generally, the density of states (DOS) and energy band structure are deemed as important parameters to describe the charge transfer ability. As shown in Fig. S2,† the valence band maximum (VBM) of bulk $BiVO_4$ is predominantly composed of O 2p and Bi 6s states, while the conduction band minimum (CBM) is mainly formed by V 3d states, which is consistent with previous reports.[33] The theoretically calculated value of the band gap is smaller than the experimental value (2.4 eV), which can be ascribed to the well-known shortcomings of the GGA functional.[34] Although the values are underestimated, the relative trend and regularity of these values are reliable.[35] As shown in Fig. 1c, the DOS of the (110) facet is more localized than that of the (101) facet. Theoretically, the increase of the overlap degree between the interacting orbitals is conducive to increasing the mobility of photogenerated carriers and promoting the separation of charges.[36] The more localized DOS indicates less overlap between interacting orbitals, implying less possibility of charge transfer and separation.[28] Therefore, the charge separation ability of {101} facets may be better than that of {110} facets. Moreover, according to Fig. 1c and the frontier orbital theory, the Bi 6s orbital plays the major role in the (010) and (101) facets, and the V 3d orbital plays the major role in the (110) facet. Thus, the charge transfer mode between (010) and (101) facets may be Bi–O–Bi, while the charge transfer mode between (010) and (110) facets may be Bi–O–V. There is hybridization between Bi 6s and O 2p orbitals (Fig. S2†), and the charge transfer between Bi and Bi is homogeneous, which makes the charge transfer in Bi–O–Bi much easier than that in Bi–O–V. Therefore, the charge transfer ability between {010} and {101} facets is stronger than that between {010} and {110} facets. Furthermore, because the drift velocity of carriers is inversely proportional to the effective mass, a lower effective mass implies more efficient charge transfer, and it is reasonable to use the effective mass to evaluate the separation ability of photogenerated electrons and holes.[37] The effective mass of electrons (m_e^*) and holes (m_h^*) of (101) and (110) facets was calculated from the curvatures of the band structures (Fig. S3†). As shown in Fig. 1d, the m_e^* and m_h^* of the (101) facet were slightly smaller than those of the (110) facet. Thus, the (101) facet has a higher charge transfer ability than the (110) facet and is more likely to reach the surface reaction sites, thereby enhancing the photocatalytic activity.

The DFT results presented above revealed that for m-$BiVO_4$, the {101} facets had stronger $BnNH_2$ adsorption ability and charge separation ability than {110} facets, stimulating us to synthesize m-$BiVO_4$ with highly exposed {101} facets.

As widely recognized, the exposed facets largely depend on the nucleation and growth behaviors along different directions during crystal growth. The colloidal synthesis method is a promising strategy, which can precisely control the size and morphology of the materials in a cost-effective and easily scaled up way.[38] Notably, reverse micelles are favorable for the synthesis of nanoparticles because they can solubilize relatively large amounts of water and the internal water core is in the nanometer range and can be controlled.[39] In addition, micelles can be deformed and change into different shapes, making it possible to synthesize crystals with different shapes.[39] Thus, a precisely controlled colloidal two-phase method was used to synthesize Q-$BiVO_4$ with highly exposed {101} facets, using oleic acid (OA) and oleylamine (OLA) as surfactants, which can form micelles in the reaction system. The reaction device used to synthesize Q-$BiVO_4$ is shown in Fig. S4.† The formation mechanism and morphology evolution of the formation process at different stages of Q-$BiVO_4$ are schematically depicted in Fig. 2. Bi^{3+} could be dissolved in the octadecene (ODE) solvent in the presence of OA and OLA. When the V^{5+} precursor was introduced into the reaction system, water-in-oil (W/O) reverse micelles could be quickly obtained. Since the solubility of Bi^{3+} in the water phase is higher than that in oil, it can be smoothly transferred to the inner aqueous cores of the reverse micelles. Thus, Bi^{3+} and V^{5+} could react rapidly to form small $BiVO_4$ nanoparticles as seeds (Fig. S5a†). Then the reverse micelles dissociated, and the surfactants selectively adsorbed on the surface of $BiVO_4$ nano-seeds, forming surfactant-$BiVO_4$ nano-seed complexes. Subsequently, the complexes self-assembled into fusiform $BiVO_4$ nanocrystals (Fig. S5b†). However, due to the mutual repulsion of the hydrophobic tails of the surfactants, the other surfactant–$BiVO_4$ nano-seed complex tended to align in the opposite direction. Meanwhile, the hydrophobic effect of the surfactant tails drove the complexes to reassemble into an ordered structure, thereby exposing different crystal facets and forming the quadrangular nanoprisms (Fig. S5c and d).† Thus, the formation of Q-$BiVO_4$ follows a "reverse micelle formation, ion transfer, seed formation, self-assembly and reassembly"

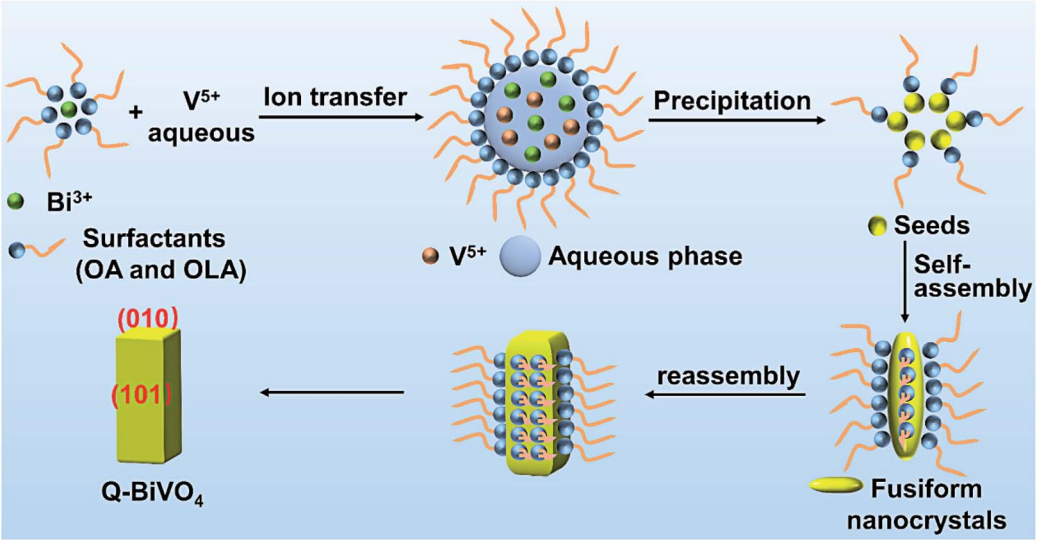

Fig. 2 Schematic illustration of the formation of monoclinic Q-$BiVO_4$ prepared through a colloidal two-phase method: reverse micelle formation, ion transfer, seed formation, self-assembly and reassembly.

process. The formation of reverse micelles and the selective adsorption, mutual repulsion, and the hydrophobic effect of surfactants provide the driving forces for the formation of Q-$BiVO_4$.

The morphology of Q-$BiVO_4$ was characterized by using a field emission scanning electron microscope (FESEM) and transmission electron microscope (TEM). As shown in Fig. 3a, b and S6,† the as-prepared Q-$BiVO_4$ has a quadrangular nanoprism shape with an average length of 200 nm, width of 100 nm and thickness of 100 nm. The detailed structures of Q-$BiVO_4$ were further investigated by high-resolution transmission electron microscopy (HRTEM). As shown in Fig. 3c and d, the

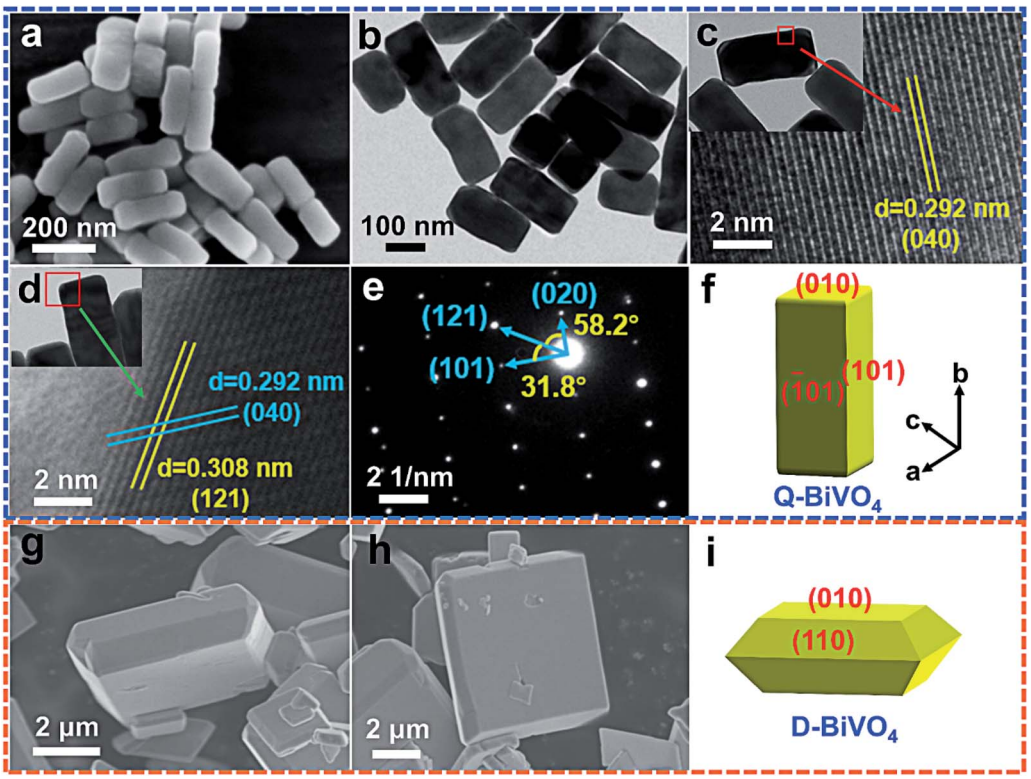

Fig. 3 (a) FESEM image of Q-$BiVO_4$. (b–d) TEM and HRTEM images of Q-$BiVO_4$. (e) The corresponding SAED pattern of Q-$BiVO_4$ (the red rectangle region in d). (f) The schematic illustration of Q-$BiVO_4$. (g and h) FESEM images of D-$BiVO_4$. (i) The schematic illustration of D-$BiVO_4$.

lattice fringes with lattice spacing of 0.292 nm and 0.308 nm are consistent with the (040) and (121) facets of m-$BiVO_4$, respectively. HRTEM images (Fig. 3c and d) exhibit a uniform grid of stripes, suggesting that Q-$BiVO_4$ has a well-crystallized structure. The clear diffraction spot with good alignment of the selected area electron diffraction (SAED) pattern indicates the single crystal structure of Q-$BiVO_4$ (Fig. 3e). The surface angle of 58.2° is consistent with the theoretical value of the angle between (020) and (121) facets of the monoclinic structure. The angle of 31.8° corresponds to the ideal angle between (101) and (121) facets of the monoclinic structure. The angle between (020) and (101) facets is 90°, which gives a direct proof that the as-prepared Q-$BiVO_4$ is regular quadrangular nanoprisms. Accordingly, other facets can be subsequently defined, as shown in Fig. 3f. Therefore, two different types of crystal facets, {010} and {101}, can be identified in Q-$BiVO_4$. The elemental mapping image of Q-$BiVO_4$ (Fig. S7†) indicates that Bi, V, and O are all uniformly distributed throughout the entire Q-$BiVO_4$. In order to explore the influence of {101} and {110} facets of m-$BiVO_4$ on the photocatalytic performance, conventional D-$BiVO_4$ was introduced as the control group. D-$BiVO_4$ was synthesized by a conventional hydrothermal method according to previous literature with some modifications.[24,40] FESEM micrographs (Fig. 3g and h) show that D-$BiVO_4$ has a decahedral morphology with the top and bottom flat surfaces defined as {010} facets, and the isosceles trapezoidal sides defined as {110} facets, respectively (Fig. 3i).[24,41] The X-ray power diffraction (XRD) pattern and Raman spectra further demonstrate the pure monoclinic phase of Q-$BiVO_4$ and D-$BiVO_4$ (JCPDS file no. 14-0688) (Fig. S8†). The chemical states of Q-$BiVO_4$ and D-$BiVO_4$ have been determined by X-ray photoelectron spectroscopy (XPS) (Fig. S9 and S10†).

The effect of {101} and {110} facets of the $BiVO_4$ samples on the photocatalytic activity was evaluated by the $BnNH_2$ oxidation experiment, which was carried out under visible light irradiation ($\lambda > 420$ nm) for 4 hours in ACN solution. Fig. 4a shows the reaction scheme for photocatalytic oxidation of $BnNH_2$ to *N*-benzylidenebenzylamine (*N*-BB) on $BiVO_4$ samples. As shown in Fig. 4b, no *N*-BB was detected in the absence of light irradiation or catalyst, indicating that the observed activities were truly from photocatalysis. In addition, according to Fig. S11,† the conversion efficiencies of the thermal reaction were significantly lower than those under light irradiation, confirming that it is light irradiation rather than the thermal process that drives the $BnNH_2$ oxidation reaction. As shown in Fig. 4b, D-$BiVO_4$ only exhibited a conversion efficiency of 48.5% with a selectivity of 95%. However, Q-$BiVO_4$ displayed a conversion efficiency of 98.3% with a selectivity of 98.7%, which was greatly enhanced under the identical conditions. The $BnNH_2$ conversion efficiency on Q-$BiVO_4$ was 2.03 fold higher than that on D-$BiVO_4$. Additionally, neither the conversion efficiency nor the selectivity on Q-$BiVO_4$ was found to be significantly decreased after five cycles (Fig. 4c). Besides, there were no obvious changes in the SEM images, XRD pattern and Raman spectra of Q-$BiVO_4$ after the cycling experiments (Fig. S12†). These results confirmed the excellent stability of Q-$BiVO_4$. More impressively, as shown in Fig. 4d, e and S13,† the detailed kinetic experiments for photocatalytic $BnNH_2$ oxidation exhibited that benzaldehyde was a reaction intermediate, which can immediately condense with $BnNH_2$ to generate *N*-BB. However, if the light irradiation time goes beyond the time required to reach 100% yield, the *N*-BB product will be over-oxidized to benzaldehyde, thus, the photocatalytic $BnNH_2$ oxidation reaction cannot reach 100% yield.

To further verify that it is the exposed crystal facets rather than the particle size or the specific surface area that are the key factor leading to differences in the photocatalytic performance of Q-$BiVO_4$ and D-$BiVO_4$, well-crystallized nano-$BiVO_4$ without the crystal facet orientation but with a similar size to Q-$BiVO_4$, was introduced for comparison. As shown in Fig. S14 and S15,† the monoclinic nano-$BiVO_4$ was irregular in shape and was an aggregate composed of 100–200 nm $BiVO_4$ nanoparticles. The chemical states of nano-$BiVO_4$ have been characterized by XPS (Fig. S16†). Notably, the $BnNH_2$ conversion efficiency of Q-$BiVO_4$ (98.3%) was 4.45 fold higher than that of nano-$BiVO_4$ (22.1%) (Fig. 4b and S17†). Additionally, the turnover frequency (TOF) of Q-$BiVO_4$ (0.786 h^{-1}) was much higher than that of nano-$BiVO_4$ (0.177 h^{-1}), D-$BiVO_4$ (0.373 h^{-1}), and some other catalysts that have been previously reported (Table S1†). Moreover, the Brunauer–Emmett–Teller (BET) specific surface areas and pore sizes of Q-$BiVO_4$ and nano-$BiVO_4$ were determined by using N_2 adsorption–desorption isotherms (Fig. S18 and Table S2†). Although nano-$BiVO_4$ has larger specific surface area than Q-$BiVO_4$, the photocatalytic activity was much lower than that of Q-$BiVO_4$. Therefore, the effect of the specific surface area was excluded. According to the Raman spectra (Fig. S19†), compared with nano-$BiVO_4$, the peak at about 830 cm^{-1} for Q-$BiVO_4$ shifts to a higher frequency, corresponding to a shorter bond length.[36] A shorter V–O bond length means greater distortion of the VO_4^{3-} tetrahedron, leading to greater overlap between the Bi 6s and O 2p orbitals, which increases the mobility of holes and promotes the separation of photogenerated electron–hole pairs. Besides, the distortion of the VO_4^{3-} tetrahedron can induce a local internal electric field, which is favorable for the separation of photogenerated carries. Therefore, the differences in the crystal structures of Q-$BiVO_4$ and nano-$BiVO_4$ lead to differences in their morphologies and exposed crystal facets, and thus cause differences in reactivity.

Furthermore, to exclude the influence of oxygen vacancies (V_O), the low-temperature electron spin resonance (ESR) spectra were obtained (Fig. 4f). The $BiVO_4$ samples exhibited the ESR signals at $g = 2.001$, which can be assigned to V_O.[42,43] However, there is little difference in the ESR signal intensity of the $BiVO_4$ samples, indicating that the difference in photocatalytic performance of the $BiVO_4$ samples is not caused by V_O.

Notably, to deeply understand the mechanism of photocatalytic $BnNH_2$ oxidation, the active species trapping experiments were carried out. 1,4-Benzoquinone (BQ), ammonium oxalate (AO) and carbon tetrachloride (CCl_4) were used as scavengers for superoxide radicals ($^{\bullet}O_2^-$), holes (h^+) and electrons (e^-), respectively.[44–47] The *N*-BB production in the presence of BQ, CCl_4 and AO is dramatically decreased (Fig. 4g), suggesting that $^{\bullet}O_2^-$, e^- and h^+ all play important roles in the photocatalytic process. As O_2 plays a crucial role in the

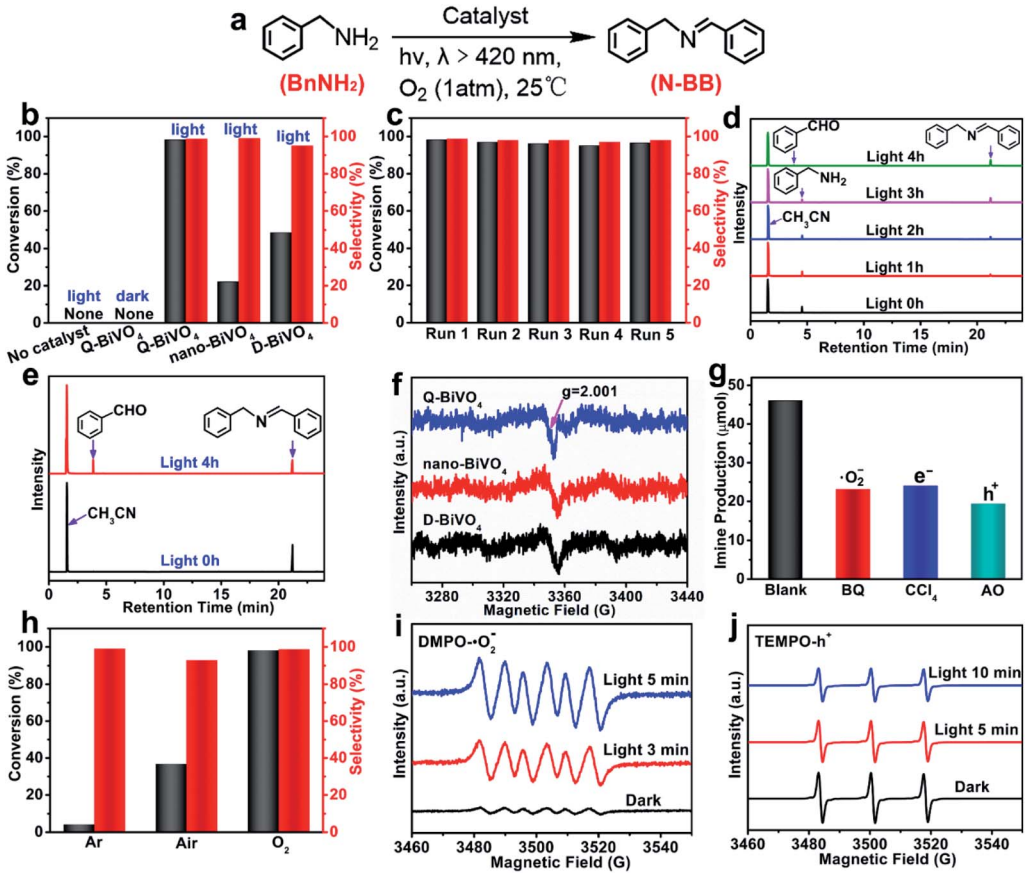

Fig. 4 (a) Reaction scheme for photocatalytic $BnNH_2$ oxidation. (b) Photocatalytic $BnNH_2$ oxidation under different conditions. (c) The stability and recyclability of Q-$BiVO_4$. (d) The complete GC-MS-FID traces for photocatalytic $BnNH_2$ oxidation on Q-$BiVO_4$ after light irradiation for different times. (e) The GC-MS-FID traces for photocatalytic *N*-BB oxidation on Q-$BiVO_4$ after light irradiation for 0 h and 4 h. Reaction conditions: 10 mg Q-$BiVO_4$, 5 mL 13.8 mM *N*-BB in ACN, 300 W Xenon lamp (λ > 420 nm), O_2 (1 atm). (f) Low-temperature ESR spectra of Q-$BiVO_4$, nano-$BiVO_4$ and D-$BiVO_4$, respectively. (g) The photocatalytic performance of Q-$BiVO_4$ in the presence of different radical scavengers. (h) The effect of different oxygen concentrations on photocatalytic performance using Q-$BiVO_4$ as the catalyst. ESR spectra of (i) DMPO-$^{\bullet}O_2^-$ and (j) TEMPO-h^+ adducts for Q-$BiVO_4$ in the dark and under light irradiation.

photocatalytic process, three experiments were carried out to investigate the effect of oxygen concentration on photocatalytic activity. As shown in Fig. 4h, Q-$BiVO_4$ in an O_2 atmosphere exhibits the highest conversion efficiency, while the conversion efficiency gradually decreases as the oxygen concentration decreases, indicating that the conversion efficiency of $BnNH_2$ is greatly dependent on the oxygen concentration. In order to further confirm the generation of these active species in the photocatalytic system, ESR tests were performed. DMPO and TEMPO were used as the spin-trapping agents to identify $^{\bullet}O_2^-$ and h^+, respectively.[47–50] Six characteristic peaks of DMPO-$^{\bullet}O_2^-$ adducts were observed in the Q-$BiVO_4$ methanol suspension under visible light irradiation, but only extremely weak signals were detected in the dark (Fig. 4i). Besides, the intensity of these characteristic peaks was significantly enhanced as the light irradiation time increased. These results confirmed the generation of $^{\bullet}O_2^-$. In addition, h^+ was also detected. The signal intensity of TEMPO-h^+ adducts was very strong in the dark (Fig. 4j). However, the intensity of these characteristic peaks gradually decreased with increasing illumination time, confirming the generation of h^+. The ESR results agreed well with the scavenging experiments (Fig. 4g).

The light-absorption ability of the catalyst is one of the main factors affecting the photocatalytic performance. UV-vis diffuse reflectance spectroscopy (DRS) was employed to characterize the band gaps and light-absorption capability of the $BiVO_4$ samples (Fig. 5a). Q-$BiVO_4$, nano-$BiVO_4$ and D-$BiVO_4$ exhibited the inherent absorption with an absorption edge at about 498 nm, 486 nm and 515 nm, respectively. According to the Kubelka–Munk function,[51] the band gap energies (E_g) of the $BiVO_4$ samples were calculated (Fig. S20†). To investigate the band structures of the samples, VB-XPS spectra were recorded (Fig. 5b). The VB-XPS of Q-$BiVO_4$, nano-$BiVO_4$ and D-$BiVO_4$ were 1.60 eV, 1.62 eV and 1.83 eV, respectively, denoting the distance between the Fermi level and valence band edge (VB). By combining the flat-band potential calculated from the Mott–Schottky plots (Fig. S21†), the valence band and conduction band were calculated. Correspondingly, the band structures of the $BiVO_4$ samples can be determined (Fig. 5c). The potential of the conduction band in $BiVO_4$ samples is more negative than

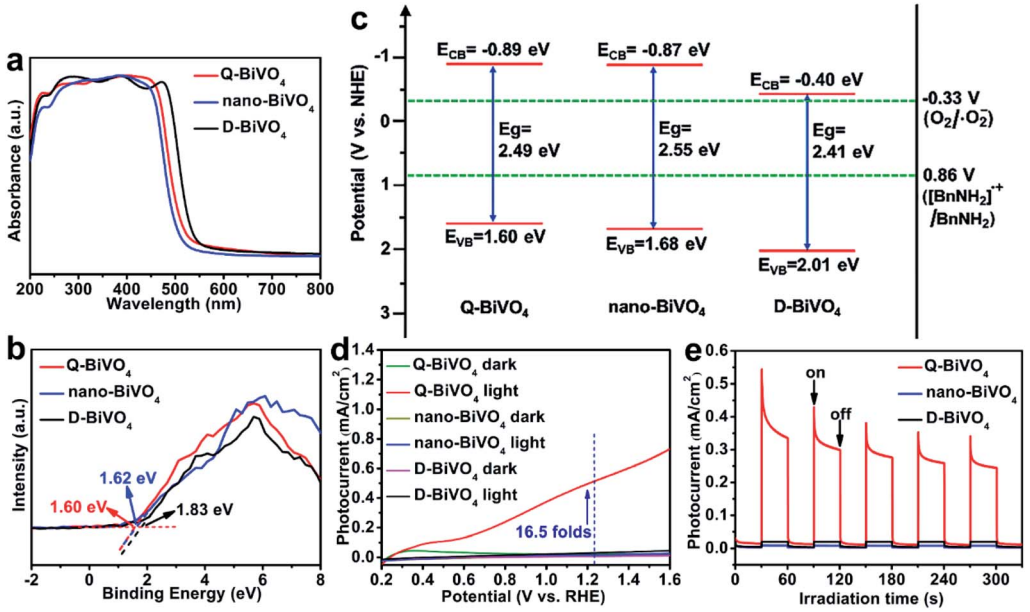

Fig. 5 (a) DRS spectra, (b) VB-XPS spectra, and (c) the band structures of Q-$BiVO_4$, nano-$BiVO_4$ and D-$BiVO_4$, respectively. (d) LSV curves of Q-$BiVO_4$, nano-$BiVO_4$ and D-$BiVO_4$ in the dark and under light irradiation. (e) Transient photocurrent responses of the $BiVO_4$ samples (all the photoelectrochemical measurements were performed by spin-coating the $BiVO_4$ samples on FTO glass substrates as the working electrode).

the standard redox potential of $O_2/{}^{\bullet}O_2^-$ (−0.33 eV *vs.* NHE[47]), so electrons in the conduction band can react with O_2 to produce ${}^{\bullet}O_2^-$. Meanwhile, the potential of the valence band in $BiVO_4$ samples is more positive than the standard redox potential of $[BnNH_2]^{\bullet+}/BnNH_2$ (0.86 V *vs.* NHE in ACN[10]), so holes in the valence band can oxidize $BnNH_2$. Thus, the $BiVO_4$ samples can induce the generation of h^+ and ${}^{\bullet}O_2^-$ radicals simultaneously, which is consistent with the active species trapping experiments and ESR results (Fig. 4).

To verify that the specific exposed facets have a great influence on the charge separation ability, photoelectrochemical measurements were carried out. The $BiVO_4$ samples were spin-coated on clean FTO glass substrates to be used as the working electrodes. As shown in Fig. 5d, Q-$BiVO_4$ exhibits a higher current density than nano-$BiVO_4$ and D-$BiVO_4$ under light irradiation. Q-$BiVO_4$ yields a photocurrent density of 0.511 mA cm^{-2} at 1.23 V_{RHE}, which is comparable to that of $BiVO_4$ samples directly grown on FTO glass substrates, and is about 30.1 and 16.5 times higher than that of nano-$BiVO_4$ (0.017 mA cm^{-2}) and D-$BiVO_4$ (0.031 mA cm^{-2}), respectively. Fig. 5e shows a comparison of the transient photocurrent response of the $BiVO_4$ samples. Conspicuously, a sharp increase of the response current over Q-$BiVO_4$ can be observed, implying the efficient separation of photogenerated electron–hole pairs on Q-$BiVO_4$. Therefore, Q-$BiVO_4$ with highly exposed {101} facets possesses excellent charge separation ability, thus, the exposed {101} facets play a crucial role in charge separation.

To further understand the effect of the exposed facets on carrier separation, it is necessary to monitor the charge transfer between Q-$BiVO_4$ and the reactant molecules. However, it is challenging to monitor the charge transfer during the $BnNH_2$ oxidation. Single-particle spectroscopy is a powerful tool to investigate the generation, transfer and recombination mechanism of carriers at the single nanoparticle level.[52–54] Notably, when charge transfer occurs, the photoluminescence (PL) intensity and lifetime will change correspondingly. Thus, the single-particle PL measurement is an ideal approach to reflect the interaction between Q-$BiVO_4$ and the reactant molecules during the photocatalytic process *in situ*. The confocal microscope system configured with a special sample cell was used (Fig. S22†). The well-dispersed Q-$BiVO_4$ was spin-coated on the clean quartz cover glasses and then the corresponding reactants were gently added to the cell. As shown in Fig. 6a and b, the PL intensity significantly decreased after adding ACN and $BnNH_2$ to the cell. Since the size of the laser spot in single-particle spectroscopy is larger than that of Q-$BiVO_4$, only the shape of the laser spot can be detected in the PL images, resulting in the morphology of Q-$BiVO_4$ measured in the PL images being inconsistent with the SEM and TEM images. Fig. 6c shows the representative PL spectra of an individual $BiVO_4$ NR at the position numbered "1". The broad PL spectra appeared in the 480–800 nm range with the center at about 650 nm, which can be ascribed to the recombination of electrons and holes trapped at the crystalline defects.[40] Compared with exposure to air, the PL intensity and peak position of the single $BiVO_4$ NR had no apparent change when ACN was dripped into the cell, while the PL intensity drastically decreased after introducing $BnNH_2$ into the system. Similar results were also obtained from other particles numbered "2" and "3" on the same quartz cover glass for Q-$BiVO_4$ (Fig. S23†). These results indicate that there is almost no charge transfer between Q-$BiVO_4$ and ACN, and ACN only acts as a solvent, but there is efficient charge transfer between Q-$BiVO_4$ and $BnNH_2$ which suppresses the radiative charge recombination in Q-$BiVO_4$. Additionally, the PL lifetime

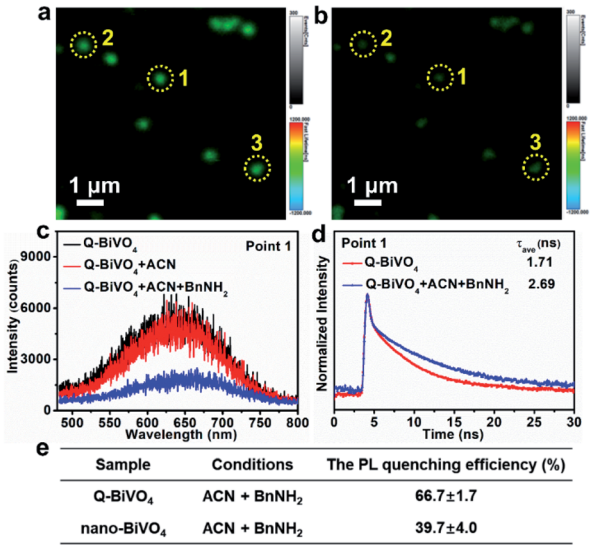

e

Sample	Conditions	The PL quenching efficiency (%)
Q-$BiVO_4$	ACN + $BnNH_2$	66.7±1.7
nano-$BiVO_4$	ACN + $BnNH_2$	39.7±4.0

Fig. 6 PL images of Q-$BiVO_4$ dispersed on quartz cover glass (a) before adding ACN and $BnNH_2$ to the cell, and (b) after adding ACN and $BnNH_2$ to the cell. (c) PL intensity spectra and (d) PL decay profiles of individual Q-$BiVO_4$ as numbered "1" in (a and b). (e) The PL quenching efficiency (%) of Q-$BiVO_4$ and nano-$BiVO_4$ after dripping ACN and $BnNH_2$ into the cell (they were calculated from the average value of the quenching efficiencies at the measuring points).

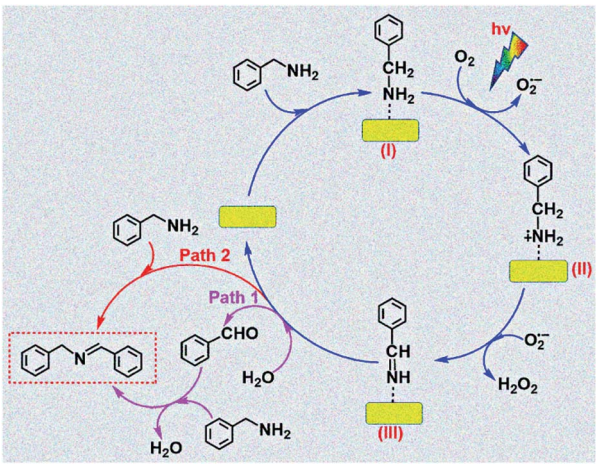

Fig. 7 Schematic illustration of the proposed feasible reaction mechanism for photocatalytic $BnNH_2$ oxidation to *N*-BB on Q-$BiVO_4$.

of a single $BiVO_4$ NR exposed to air is 1.71 ns, while it becomes 2.69 ns after adding ACN and $BnNH_2$ to the cell (Fig. 6d), further confirming the efficient charge transfer between Q-$BiVO_4$ and $BnNH_2$. Moreover, to further confirm the importance of the specific exposed facets in carrier separation, the single-particle PL spectra of irregular nano-$BiVO_4$ were measured. After adding ACN and $BnNH_2$ to the cell, the PL intensity of nano-$BiVO_4$ decreased slightly (Fig. S24†). When ACN and $BnNH_2$ were dripped into the system, the PL intensity of nano-$BiVO_4$ was quenched by about 39.7%, which was much lower than the PL quenching efficiency of Q-$BiVO_4$ (66.7%) (Fig. 6e), indicating that the carriers were more efficiently separated in Q-$BiVO_4$ and there are more photogenerated holes reacting with $BnNH_2$ in Q-$BiVO_4$ to give a higher conversion efficiency for photocatalytic $BnNH_2$ oxidation than in nano-$BiVO_4$, corresponding to the photocatalytic $BnNH_2$ oxidation performance (Fig. S17†). The thickness of D-$BiVO_4$ is in the micron level, and it is difficult for laser focusing, which may result in inaccurate test results, thus the single-particle PL spectra of D-$BiVO_4$ were not measured.

Based on the above results and analysis, a plausible mechanism was proposed for the photocatalytic $BnNH_2$ oxidation on Q-$BiVO_4$ as illustrated in Fig. 7. $BnNH_2$ molecules can be well adsorbed on the surface of Q-$BiVO_4$ to form a surface complex (I). Under visible light irradiation, Q-$BiVO_4$ is excited to generate electron–hole pairs. The adsorbed $BnNH_2$ molecules are oxidized by photogenerated holes in the valence band to produce benzylamine cation-radical (II). Oxygen molecules react with photogenerated electrons in the conduction band to produce superoxide radicals ($^{\bullet}O_2^-$), and then the intermediate II reacts with $^{\bullet}O_2^-$ to form the phenylmethanimine intermediate (III) and H_2O_2.[12,55] The formation of H_2O_2 during the photocatalytic process was confirmed by iodometry (Fig. S25†). The intermediate III will be hydrolyzed by trace amounts of water generated during the reaction and subsequently convert to benzaldehyde, which can further condense with $BnNH_2$ to generate the desired *N*-BB (Fig. S13b†).[2] The intermediate III may also couple with another $BnNH_2$ molecule to form the corresponding *N*-BB.[12]

Conclusions

In summary, the preparation of monoclinic Q-$BiVO_4$ with highly exposed {101} facets was realized by a precisely-controlled colloidal two-phase method. The as-prepared Q-$BiVO_4$ exhibited superior photocatalytic activity with a $BnNH_2$ conversion efficiency of 98.3%, about 2.03 fold higher than that of D-$BiVO_4$. The photocurrent density of Q-$BiVO_4$ was 0.511 mA cm^{-2} at 1.23 V_{RHE}, about 16.5 times higher than that of D-$BiVO_4$. DFT calculations and the experimental results demonstrate that the excellent activity of Q-$BiVO_4$ comes from several synergetic effects. First, the strong $BnNH_2$ adsorption ability of {101} facets promotes the subsequent $BnNH_2$ oxidation process. Moreover, a greater overlap degree between the interacting orbitals, the lighter effective masses of photogenerated electrons and holes of {101} facets, and the Bi–O–Bi charge transfer mode between {101} and {010} facets contribute to the significantly enhanced charge separation efficiency. More importantly, the interaction between Q-$BiVO_4$, ACN and $BnNH_2$ was explored *in situ* by using the single-particle PL spectra, indicating that ACN only acts as a solvent and there is efficient charge transfer between Q-$BiVO_4$ and $BnNH_2$. This work provides a deep understanding of the interaction between Q-$BiVO_4$ and the reactant molecules, and offers guidance to design efficient and morphology-tailored photocatalysts for organic transformations.

Author contributions

M. L. designed and performed the experiments, and wrote the paper. Z. Z. supervised the project and revised the manuscript. All authors analyzed and discussed the experimental results.

Conflicts of interest

There are no conflicts to declare.

Acknowledgements

This work was financially supported by the Natural Science Foundation of Shandong Province (ZR2021JQ06), National Natural Science Foundation of China (No. 22072072), National Key Research and Development Program of China (2020YFA0710301), Shandong University Multidisciplinary Research and Innovation Team of Young Scholars (2020QNQT11, and 2020QNQT012), Qilu Young Scholars and Outstanding Young Scholars Projects of Shandong University, and Taishan Scholar Foundation of Shandong Province.

References

1 X. Lang, H. Ji, C. Chen, W. Ma and J. Zhao, *Angew. Chem., Int. Ed.*, 2011, **50**, 3934–3937.
2 S. Furukawa, Y. Ohno, T. Shishido, K. Teramura and T. Tanaka, *ACS Catal.*, 2011, **1**, 1150–1153.
3 B. Yuan, R. Chong, B. Zhang, J. Li, Y. Liu and C. Li, *Chem. Commun.*, 2014, **50**, 15593–15596.
4 R. D. Patil and S. Adimurthy, *Asian J. Org. Chem.*, 2013, **2**, 726–744.
5 E. Guiu, B. Munoz, S. Castillon and C. Claver, *Adv. Synth. Catal.*, 2003, **345**, 169–171.
6 K. C. Nicolaou, C. J. N. Mathison and T. Montagnon, *Angew. Chem., Int. Ed.*, 2003, **42**, 4077–4082.
7 T. Mukaiyama, A. Kawana, Y. Fukuda and J. Matsuo, *Chem. Lett.*, 2001, **30**, 390–391.
8 K. C. Nicolaou, C. J. N. Mathison and T. Montagnon, *J. Am. Chem. Soc.*, 2004, **126**, 5192–5201.
9 S. Zavahir and H. Zhu, *Molecules*, 2015, **20**, 1941–1954.
10 A. D. Proctor, S. Panuganti and B. M. Bartlett, *Chem. Commun.*, 2018, **54**, 1101–1104.
11 F. Su, S. C. Mathew, L. Moehlmann, M. Antonietti, X. Wang and S. Blechert, *Angew. Chem., Int. Ed.*, 2011, **50**, 657–660.
12 J. Yang and C.-Y. Mou, *Appl. Catal., B*, 2018, **231**, 283–291.
13 C. Mao, H. Cheng, H. Tian, H. Li, W.-J. Xiao, H. Xu, J. Zhao and L. Zhang, *Appl. Catal., B*, 2018, **228**, 87–96.
14 A. Han, H. Zhang, G.-K. Chuah and S. Jaenicke, *Appl. Catal., B*, 2017, **219**, 269–275.
15 P. Li, X. Chen, H. He, X. Zhou, Y. Zhou and Z. Zou, *Adv. Mater.*, 2018, **30**, 1703119.
16 M.-Y. Ye, Z.-H. Zhao, Z.-F. Hu, L.-Q. Liu, H.-M. Ji, Z.-R. Shen and T.-Y. Ma, *Angew. Chem., Int. Ed.*, 2017, **56**, 8407–8411.
17 M. Huang, Z. Huang and H. Zhu, *Nano Energy*, 2020, **70**, 104487.
18 T. Liu, X. Zhang, F. Zhao and Y. Wang, *Appl. Catal., B*, 2019, **251**, 220–228.
19 Q. Zhang, M. Liu, W. Zhou, Y. Zhang, W. Hao, Y. Kuang, H. Liu, D. Wang, L. Liu and J. Ye, *Nano Energy*, 2021, **81**, 105651.
20 S. Chen, D. Huang, P. Xu, X. Gong, W. Xue, L. Lei, R. Deng, J. Li and Z. Li, *ACS Catal.*, 2020, **10**, 1024–1059.
21 J. H. Baek, T. M. Gill, H. Abroshan, S. Park, X. Shi, J. Norskoy, H. S. Jung, S. Siahrostami and X. Zheng, *ACS Energy Lett.*, 2019, **4**, 720–728.
22 K. Zhang, Y. Liu, J. Deng, S. Xie, X. Zhao, J. Yang, Z. Han and H. Dai, *Appl. Catal., B*, 2018, **224**, 350–359.
23 C. Dong, S. Lu, S. Yao, R. Ge, Z. Wang, Z. Wang, P. An, Y. Liu, B. Yang and H. Zhang, *ACS Catal.*, 2018, **8**, 8649–8658.
24 R. Li, F. Zhang, D. Wang, J. Yang, M. Li, J. Zhu, X. Zhou, H. Han and C. Li, *Nat. Commun.*, 2013, **4**, 1432.
25 C. W. Kim, Y. S. Son, M. J. Kang, D. Y. Kim and Y. S. Kang, *Adv. Energy Mater.*, 2016, **6**, 1501754.
26 Y. Qi, Y. Zhao, Y. Gao, D. Li, Z. Li, F. Zhang and C. Li, *Joule*, 2018, **2**, 2393–2402.
27 J. Hu, H. He, L. Li, X. Zhou, Z. Li, Q. Shen, C. Wu, A. M. Asiri, Y. Zhou and Z. Zou, *Chem. Commun.*, 2019, **55**, 4777–4780.
28 J. Yang, D. Wang, X. Zhou and C. Li, *Chem.–Eur. J.*, 2013, **19**, 1320–1326.
29 Y. Qi, J. Zhang, Y. Kong, Y. Zhao, S. Chen, D. Li, W. Liu, Y. Chen, T. Xie, J. Cui, C. Li, K. Domen and F. Zhang, *Nat. Commun.*, 2022, **13**, 484.
30 A. J. E. Rettie, H. C. Lee, L. G. Marshall, J.-F. Lin, C. Capan, J. Lindemuth, J. S. McCloy, J. Zhou, A. J. Bard and C. B. Mullins, *J. Am. Chem. Soc.*, 2013, **135**, 11389–11396.
31 W. Wang, Y. Wang, R. Yang, Q. Wen, Y. Liu, Z. Jiang, H. Li and T. Zhai, *Angew. Chem., Int. Ed.*, 2020, **59**, 16974–16981.
32 F. Ma, S. Wang, L. Han, Y. Guo, Z. Wang, P. Wang, Y. Liu, H. Cheng, Y. Dai, Z. Zheng and B. Huang, *ACS Appl. Mater. Interfaces*, 2021, **13**, 56140–56150.
33 A. Kudo, K. Omori and H. Kato, *J. Am. Chem. Soc.*, 1999, **121**, 11459–11467.
34 J. P. Perdew and M. Levy, *Phys. Rev. Lett.*, 1983, **51**, 1884–1887.
35 J. Zhang, F. Ren, M. Deng and Y. Wang, *Phys. Chem. Chem. Phys.*, 2015, **17**, 10218–10226.
36 J. Yu and A. Kudo, *Adv. Funct. Mater.*, 2006, **16**, 2163–2169.
37 W. Yu, J. Zhang and T. Peng, *Appl. Catal., B*, 2016, **181**, 220–227.
38 C. Tan and H. Zhang, *Nat. Commun.*, 2015, **6**, 7873.
39 C. Burda, X. B. Chen, R. Narayanan and M. A. El-Sayed, *Chem. Rev.*, 2005, **105**, 1025–1102.
40 T. Tachikawa, T. Ochi and Y. Kobori, *ACS Catal.*, 2016, **6**, 2250–2256.
41 Y. Zhao, C. Ding, J. Zhu, W. Qin, X. Tao, F. Fan, R. Li and C. Li, *Angew. Chem., Int. Ed.*, 2020, **59**, 9653–9658.
42 H. Wang, D. Yong, S. Chen, S. Jiang, X. Zhang, W. Shao, Q. Zhang, W. Yan, B. Pan and Y. Xie, *J. Am. Chem. Soc.*, 2018, **140**, 5320.
43 H. Li, J. Li, Z. Ai, F. Jia and L. Zhang, *Angew. Chem., Int. Ed.*, 2018, **57**, 122–138.
44 H. Wang, S. Chen, D. Yong, X. Zhang, S. Li, W. Shao, X. Sun, B. Pan and Y. Xie, *J. Am. Chem. Soc.*, 2017, **139**, 4737–4742.
45 X. Zhao, Y. You, S. Huang, Y. Wu, Y. Ma, G. Zhang and Z. Zhang, *Appl. Catal., B*, 2020, **278**, 119251.
46 Y. Nosaka and A. Y. Nosaka, *Chem. Rev.*, 2017, **117**, 11302–11336.
47 Y. Xue, Z. Wu, X. He, Q. Li, X. Yang and L. Li, *J. Colloid Interface Sci.*, 2019, **548**, 293–302.

48 J. Wang, Y. Yu and L. Zhang, *Appl. Catal., B*, 2013, **136**, 112–121.
49 K. Huang, T. Hu and Y. Wang, *J. Solid State Chem.*, 2021, **294**, 121864.
50 F. Ye, H. Li, H. Yu, S. Chen and X. Quan, *Appl. Catal., B*, 2018, **227**, 258–265.
51 C. Zhou, Y. Zhao, L. Shang, R. Shi, L.-Z. Wu, C.-H. Tung and T. Zhang, *Chem. Commun.*, 2016, **52**, 8239–8242.
52 X. Shi, S. Kim, M. Fujitsuka and T. Majima, *Appl. Catal., B*, 2019, **254**, 594–600.
53 Y. Xiao, J. Hong, X. Wang, T. Chen, T. Hyeon and W. Xu, *J. Am. Chem. Soc.*, 2020, **142**, 13201–13209.
54 J. Xue, O. Elbanna, S. Kim, M. Fujitsuka and T. Majima, *Chem. Commun.*, 2018, **54**, 6052–6055.
55 S. Boochakiat, D. Tantraviwat, O. Thongsook, S. Pornsuwan, A. Nattestad, J. Chen, D. Channei and B. Inceesungvorn, *J. Colloid Interface Sci.*, 2021, **602**, 168–176.